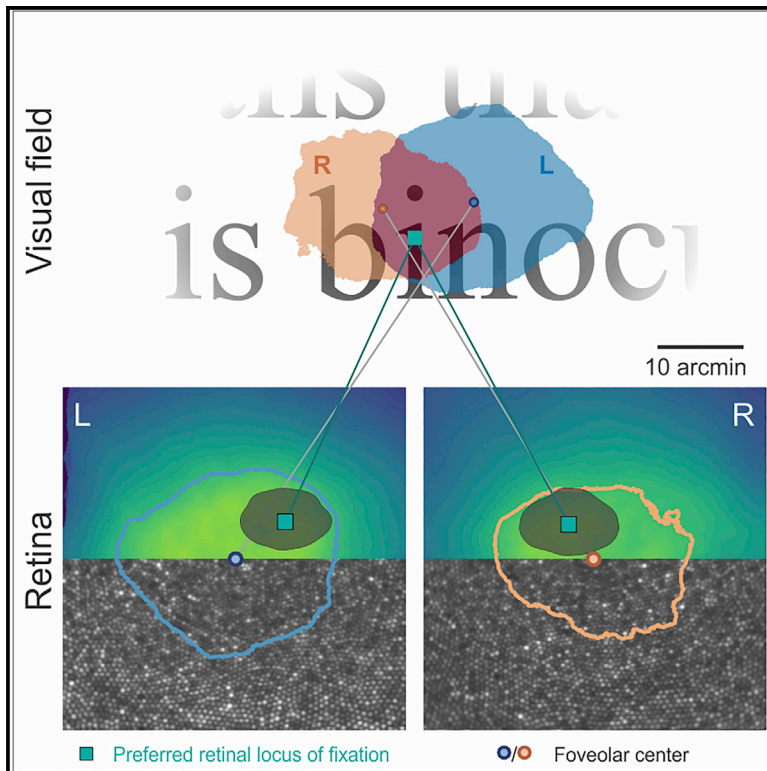


Current Biology

Human gaze is systematically offset from the center of cone topography

Graphical abstract



Authors

Jenny L. Reiniger, Niklas Domdei,
Frank G. Holz, Wolf M. Harmening

Correspondence

wolf.harmening@ukbonn.de

In brief

Reiniger et al. show that the preferred retinal locus of fixation is systematically and reproducibly displaced from the topographical center of the human fovea. In the binocular visual field, the area of high cone density sampling is thus horizontally enlarged and offset toward an area usually containing smaller details in the natural environment.

Highlights

- Foveal cone topography is mirror symmetric between fellow eyes
- The preferred retinal locus of fixation (PRL) is reproducible over multiple years
- The PRL is offset naso-superiorly on the retina, correlated between fellow eyes
- The binocular area of high cone densities is horizontally enlarged, on average

Report

Human gaze is systematically offset from the center of cone topography

Jenny L. Reiniger,¹ Niklas Domdei,¹ Frank G. Holz,¹ and Wolf M. Harmening^{1,2,*}

¹Rheinische Friedrich-Wilhelms-Universität Bonn, Department of Ophthalmology, Ernst-Abbe-Str. 2, Bonn 53127, Germany

²Lead contact

*Correspondence: wolf.harmening@ukbonn.de

<https://doi.org/10.1016/j.cub.2021.07.005>

SUMMARY

The small physical depression of the human retina, the fovea, is the retinal locus of prime visual resolution, achieved by a peaking topography of the light-sensitive cone photoreceptor outer segments^{1–3} and a post-receptor wiring scheme preserving high-density sampling.^{4,5} Humans dynamically direct their gaze such that the retinal images of objects of interest fall onto the foveola, the central one-degree diameter of the fovea,^{6–8} but it is yet unclear whether a relationship between the individual photoreceptor topography at this location and visual fixation behavior exists.^{9,10} By employing adaptive optics *in vivo* imaging and micro-stimulation,^{11–13} we created topographical maps of the complete foveolar cone mosaics in both eyes of 20 healthy participants while simultaneously recording the retinal location of a fixated visual object in a psychophysical experiment with cellular resolution. We found that the locus of fixation was systematically shifted away from the topographical center toward a naso-superior quadrant on the retina, about 5 min of arc of visual angle on average, with a mirror symmetrical trend between fellow eyes. In cyclopean view, the topographical centers were superior to the fixated target, corresponding to areas in the visual field usually more distant^{14,15} and thus containing higher spatial frequencies. Given the large variability in foveal topography between individuals, and the surprising precision with which fixation is repeatedly directed to just a small bouquet of cones in the foveola, these findings demonstrate a finely tuned, functionally relevant link between the development of the cellular mosaic of photoreceptors and visual behavior.

RESULTS AND DISCUSSION

Foveolar cone topography

By high-resolution adaptive optics scanning laser ophthalmoscopy (AOSLO), cone photoreceptor topography at the very center of the fovea was analyzed in 41 eyes of 21 healthy human participants (twenty binocular and one monocular). In each retinal image, about 6,800 to 9,100 cones were marked and their location used to compute continuous two-dimensional maps of cone density (STAR Methods; Figures 1A–1F). Peak cone density (PCD) varied widely across participants (range: 10,823–18,023; average: 14,067 cones/deg²; see also Table S1), similar to previous reports.^{1,2,9,10,16–19} In alignment with histology³ and *in vivo* imaging,^{2,17} we found a steeper drop in cone density along the vertical compared to the horizontal meridian (Figures 1G and 1H), an anisotropy also found in retinas of other mammals.^{20,21}

Cone density, interocular symmetry, and fixation behavior (see below) of the three children in our study (aged 10, 12, and 14 years; participants P3, P10, and P16, respectively) did not differ from the adult population. This extends cone density reports at higher eccentricities^{22,23} into the foveal center. Histological studies point to an earlier cessation of centripetal cone photoreceptor migration, with a doubling of cone density between gestational week 22 and postnatal day 5, and a tripling

between 5 days and 45 months postnatal.²⁴ Visual acuity in children was shown to approach adult performance between the ages of 5 and 6 years.²⁵ Thus, the children examined here are assumed to be in a comparable stage of visual development as adults.

We introduce a novel, spatially more robust metric to anchor the fovea's topographical center: the cone density centroid (CDC) was computed as the weighted center of cone densities within the 20th percentile contour (Figure 1F). In 8 participants (16 eyes), foveolar cone mosaics were imaged and analyzed on two different days. After careful alignment of high signal-to-noise ratio images, the advantage of using the CDC over PCD location as anchor became apparent. While the PCDs as well as CDC densities were highly correlated between fellow eyes ($r^2 = 0.95$, $p \ll 0.001$ and $r^2 = 0.89$, $p \ll 0.001$, respectively; Figure 1I), on average, PCD locations varied by more than 3-fold (mean \pm SD: 3.0 ± 2.3 arcmin; range: 0.1–7.9 arcmin), compared to CDC locations (mean \pm SD: 0.9 ± 0.7 arcmin; range: 0.1–2.6 arcmin; $p = 0.002$; paired t test). In all following analyses, the CDC was used as the singular spatial reference location of the foveolar center.

The fact that more and more optical and analytical limitations are lifted with novel imaging techniques, like lateral resolution exceeding the diffraction limit offered by AOSLO,²⁶ and the good agreement between *in vivo* studies are likely to lead toward

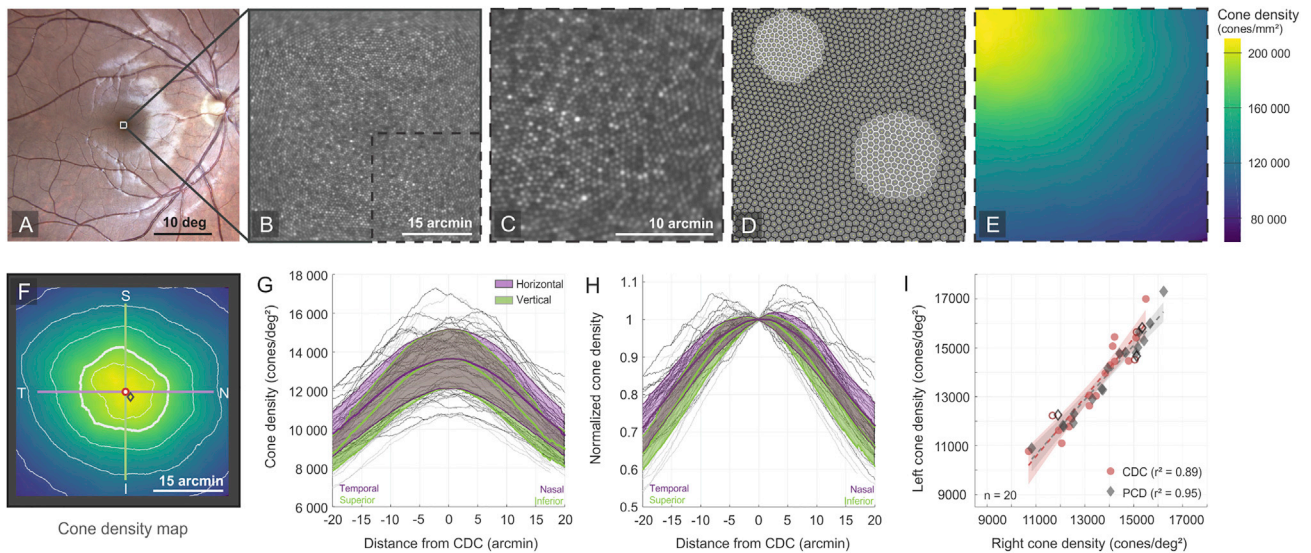


Figure 1. Cellular topography of the foveola

(A) Fundus photograph of a participant's right eye.
 (B and C) AOSLO image of the foveal center (B), dashed outline enlarged in (C).
 (D) Cone density was computed by the encircled area of the nearest 150 Voronoi tiles around each image pixel (two examples shown).
 (E) Cone density color coded as cones/mm².
 (F) In the full map, iso-contour lines are 10th, 20th (bold), 40th, 60th, and 80th percentiles. Diamond, peak cone density (PCD); red circle, cone density centroid (CDC). See [Figure S1](#) for maps of all eyes. Green and purple lines are cardinal meridians shown in (G) and (H) for all eyes.
 (G) Individual (thin) and average (bold) profiles of absolute cone density.
 (H) Same as (G), normalized to the cone density at the CDC.
 (I) Cone densities at the CDC (circles) and PCDs (diamond) were highly correlated between fellow eyes. Open markers indicate children. Regression lines and 95% confidence intervals are represented by dotted lines and shaded areas, respectively.
 See [Figure S2](#) for extended symmetry analysis.

a replacement of the gold standard for quantitative cone mosaic analysis, from histology of dissected tissue preparations³ toward high-resolution *in vivo* imaging.

Interocular symmetry of foveolar topography

Symmetry is an extensively studied characteristic in various organs. Previous observations in the field of ophthalmic optics showed ocular symmetries between fellow eyes, such as corneal topography and ocular wavefront aberrations.²⁷ For cone density, high interocular correlation was shown at larger retinal eccentricities (250, 420, 760, and 1,300 μm)²⁸ as well as for PCD.¹⁷ In the foveal center, similar as shown in our data, Cava et al.¹ found that, in addition to the PCD, Voronoi cell area regularity and certain iso-density contour areas are also highly symmetrical between fellow eyes. Here, we observed high topographical symmetry between fellow eyes, readily perceivable by eye ([Figure S1](#)). When the pointwise difference in density was computed between fellow eyes, the median root-mean-square (RMS) (3.8%) was only slightly larger than the difference between two maps of the same eye analyzed from different days (median RMS: 2.9%; [Figure S2](#)). Small local image distortions are likely to occur due to the scanning nature of the AOSLO, pixelwise image acquisition, and sequential stabilization processes. With a conservative estimation of such local distortions of up to 3 pixels (equaling 0.3 minutes of arc of visual angle), they remain relatively small compared to the magnitude of measured offsets between retinal locations of interest. By manually selecting a reference

frame with low distortions ([STAR Methods](#)), we further minimized this confound. PCDs in fellow eyes were strongly correlated and not different between right and left eyes (paired t test; $p = 0.6$), as is also observed by Cava et al.¹ There was also no significant difference of PCDs between dominant and non-dominant eyes in our population (paired t test; $p = 0.4$). Preliminary data from an acuity study of our group, including pilot data of five participants from the present study, showed that resolution acuity was better in the dominant eyes of all five examined participants, while acuity thresholds were highly correlated with the density of the foveolar cone mosaic.²⁹ This suggests that better performance in the dominant eye might be related to other factors than PCD, e.g., the particular retinal locations used during the task as well as retinal motion. To test this hypothesis, resolution acuity and ocular dominance need to be investigated in a larger population. Additionally, a spatially resolved analysis of retinal image quality might help to better understand how optical limits during development influence the formation of the optimal retinal locus, as they affect the sampling limit in resolution tasks.³⁰

Preferred retinal locus of fixation

In the natural environment, fixation, discrimination, or resolution requirements are often closely related. For a long time, it was common view that the anatomical center of the fovea also represents the center of fixation,³¹ a view supported by the rough alignment between these retinal loci. With current imaging techniques, however, opening the door to the exact cellular makeup

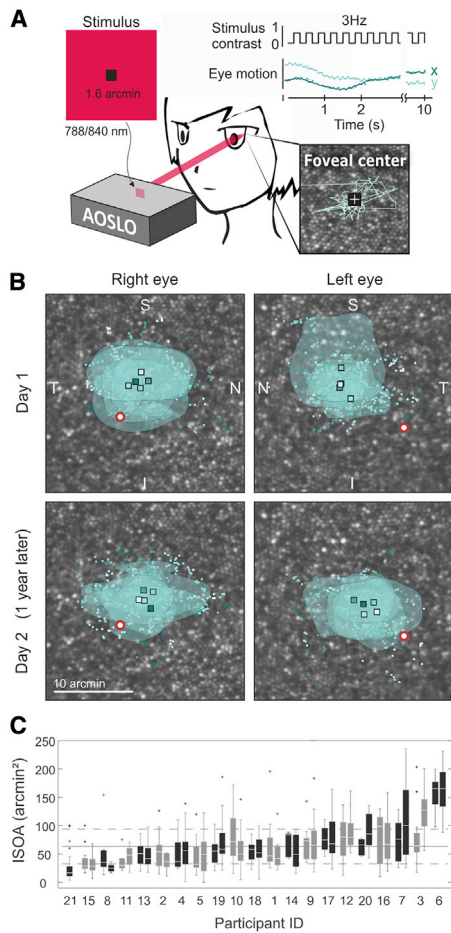


Figure 2. Measuring fixation behavior

(A) Unambiguous retinal landing points of a small flashing target were derived from multiple AOSLO videos.
 (B) The PRLs (squares) of consecutive videos in right and left eyes of P5 on two different days (~1 year between measurements; see Figure S3 for fixation stability across multiple years). Small dots are all stimulus locations; marker brightness represents consecutive videos. Contours are the area containing one standard deviation of the data (isoline area [ISOA]). Red circle, CDC.
 (C) ISOAs in all fellow eyes, participants ordered by average magnitude. The left bars represent left and right bars right eyes, respectively. Horizontal lines represent the average (solid) \pm one standard deviation (dotted). Box whisker extends to the most extreme data values, and plus markers represent outliers (distance $>1.5 \times$ range between 25th and 75th percentiles).

of an individual eye, it was revealed that the preferred retinal locus of fixation (PRL) is offset from the location of PCD as well as from the center of the foveal avascular zone and foveal pit.^{2,9,10,16,32} The PRL is also not the retinal location that provides highest sensitivity to small spot stimuli, which was recently shown to be rather plateau-like within the central 0.1 degree of the foveola.³³ However, a possible systematic relationship between the PRL and the retinal cone mosaic was yet missing.

In the majority of eyes in our population (33/41), fixation behavior was examined on 2 or more days (Table S1). PRLs could be found accurately, with a median distance of 2.3 arcmin between consecutive measurements (range: 1.0–5.6 arcmin; Figures 2B and S3B). When stimulus locations were pooled

across a single day, median locations differed by only 1.5 arcmin (range: 1.0–4.2 arcmin; Figures S3A and S3B). The observed fixation stability, given by the isoline areas (ISOAs), ranged between 23 and 153 arcmin² in right eyes and between 29 and 154 arcmin² in left eyes (Table S1). The participants who had a larger median ISOA also had higher PRL variability between single measurements ($\rho = 0.39$; $p = 0.01$; Figure 2C). PRLs as well as ISOAs were highly reproducible in individuals, even across a period of up to 3.5 years (Figure S3A). This confirms and extends the finding of Kilpeläinen et al.,³² showing PRL reproducibility over a period of 2 days, on average.

In addition to the previously described structural symmetry between fellow eyes, we also observed functional symmetries. Albeit recorded under monocular viewing, fixation stability across fellow eyes was highly correlated ($r^2 = 0.66$; $p < 0.001$; Figure 2C), supporting the hypothesis of an underlying coupling of both eyes during fixation.³⁴ When eyes were grouped according to ocular dominance, there was no difference between median ISOAs of dominant and non-dominant eyes ($p = 0.062$; Wilcoxon signed rank test; $n = 20$). Previous studies found functional interocular correlation in microsaccade rates and amplitudes under monocular viewing conditions³⁵ and bivariate contour ellipse areas³⁶ and suggest improved fixation stability under binocular viewing conditions.^{34,35}

The relationship of cone topography and fixation

By measuring fixation behavior in a cone-resolved experiment (Figures 2A and 2B) and by careful alignment with the cone density maps of both eyes, we reveal a fine and very reproducible systematic offset between cone topography and fixation behavior. In retinal coordinates, the PRL was displaced naso-superiorly from the CDC by an average amount of 4.7 arcmin (Figure 3A), corresponding to about 10 cone diameters, in accordance with a recent monocular study comparing PRL and PCD locations.³² Offset distances were correlated between fellow eyes in our study ($r^2 = 0.45$; $p = 0.001$; Figure S4B), with high correlation in the vertical ($r^2 = 0.72$; $p < 0.001$; Figure 3B), but not horizontal component ($r^2 = 0.09$; $p = 0.19$). The offset's angular component was thus not significantly correlated ($r^2 = 0.07$; $p = 0.28$), albeit with a mirror symmetrical trend along a vertical axis (Figure S4C). Other studies, with a lower number of subjects or a less accurate method of measuring the PRL, found larger offsets with median values of 9.8 and 11.5 arcmin.^{9,10} However, a trend toward PRL formation superior to the PCD is visible also in those data. Similar PRL offsets (mean: 5.3 arcmin) could be found when re-analyzing data from Wang et al.² with our analysis methods (Figure S4A).

Projection of cone topography into the visual field

In the following, we assume that monocular and binocular PRLs are identical and that PRLs are retinal coordinates of corresponding points in the visual environment and thus independent of viewing distance.³⁷ In a cyclopean view, where both PRLs are the common center, CDCs and high cone density areas were slightly superior to the fixated point (Figures 4A and 4B), firmly linked between the two eyes. In a natural environment, the visual field above a fixated point is often farther away (e.g., horizontal surfaces, such as grounds and table tops),^{14,15} creating a bottom-to-top gradient of spatial frequencies with higher frequencies above the point of fixation. A displacement of the CDC superior to fixation might allow for a better estimation of

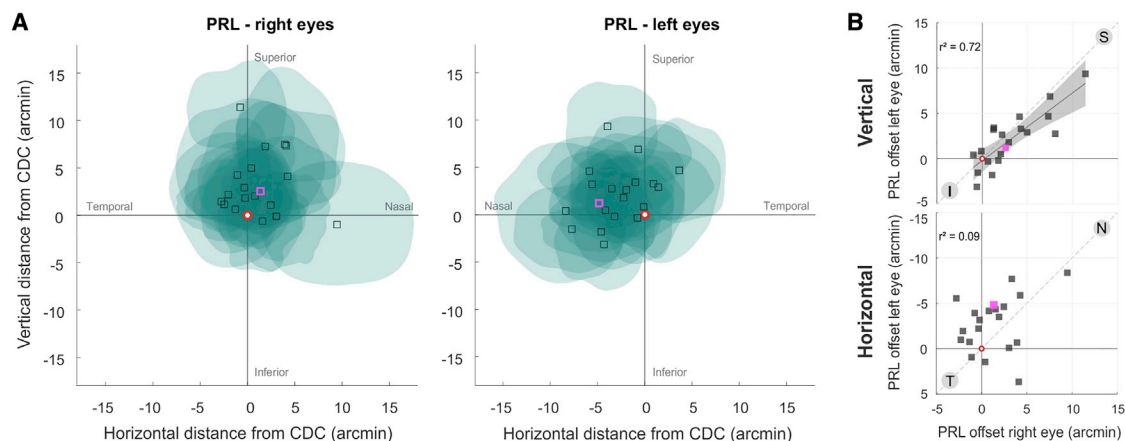


Figure 3. Relationship between cone topography and PRL in retinal coordinates

(A) Right and left eyes' median PRL and 1 SD ISOAs plotted relative to the CDC (see also Figure S4). Exemplary data pair most similar to average (P13) is highlighted in purple.

(B) Vertical offsets were strongly correlated between fellow eyes ($r^2 = 0.72$; $p < 0.001$). The linear regression and 95% confidence interval (shaded area) are shown. Horizontal offsets were not correlated ($r^2 = 0.09$; $p = 0.19$). I, inferior; N, nasal; S, superior; T, temporal retinal orientations.

See Figure S4 for distance and angular relationships.

3D structure of textured surfaces or objects. Due to the strong correlation of the vertical position in the visual field, the offset between both eyes' CDCs was more pronounced horizontally in our data (Figures 4C and 4D). Also, CDCs of most right eyes landed leftward from the left eye's CDCs, resulting in crossed disparity. Uncrossed disparities were observed in five participants only, who also had minimal horizontal offsets. Figure 4D further illustrates the geometry and magnitude of the offsets projected into the binocular field of view.

The highly ordered and systematic functional and topographical architecture we observe between fellow eyes could be the result of a developmental process creating appropriate location information for binocular spatial sampling. From such point of view, a nasal displacement might emerge as an “overshoot” during PRL formation, ensuring overlap between the high spatial frequency sampling capacity areas in both eyes. We found incomplete overlaps that essentially enlarge the visual field sampled by high-density cones in all participants (Figures 4B and 4C). By the rules of binocular combination, the eye that sees higher contrast and sharper details gets more weight in the cyclopean percept.³⁸ Thus, by imperfect horizontal alignment of cone topographies, the visual system might create a larger field of sharp perception with individual sharpness gradients of the two retinal images.³⁹

One of the factors driving the enrichment of visual capacities during development is the demand of resolving fine structures in the visual environment, and fixation behavior seems to contribute to such strategies. In adults, fixational eye motion was shown to enhance visual resolution, for instance.^{40–42} Post-receptorally, the connectivity between individual cones and midget bipolar and ganglion cells was recently shown to develop and establish a private line for the central photoreceptors already during gestation.⁴ The centripetal migration of cone photoreceptors starts in parallel but takes place mainly after birth.²⁴ The nasal superior offset direction aligns with the closest connectivity to the optic nerve head, which could facilitate the slightly offset PRL

development, even if conduction velocity of retinal ganglion cells was shown to minimize possible time differences across the retina.⁴³ At larger retinal eccentricities, midget ganglion cells have smaller dendritic field diameters in the nasal quadrant of human retinae,⁴⁴ which may be an outcome of the same underlying mechanisms as the biased PRL formation.

Conclusions

Taken together, participants without known retinal disease or abnormalities showed a small but systematic offset between their PRL and the center of cone density distribution, formed in a way to vertically offset high cone densities toward the superior part of the visual field and to ensure a horizontal overlap of those areas in the binocular visual field. This functional symmetry was associated with high interocular symmetry of foveolar cone topography. Binocular, foveated display systems that seek to mimic human vision with high precision could be tuned to reflect this spatial relationship.⁴⁵ Binocular *in vivo* foveal topography data may provide a basis for detecting changes in the central photoreceptor topography during retinal disease⁴⁶ and, more generally, could contribute to replace histology as gold standard for normative human photoreceptor evaluations in a healthy population.

STAR★METHODS

Detailed methods are provided in the online version of this paper and include the following:

- KEY RESOURCES TABLE
- RESOURCE AVAILABILITY
 - Lead contact
 - Materials availability
 - Data and code availability
- EXPERIMENTAL MODEL AND SUBJECT DETAILS
 - Human participants

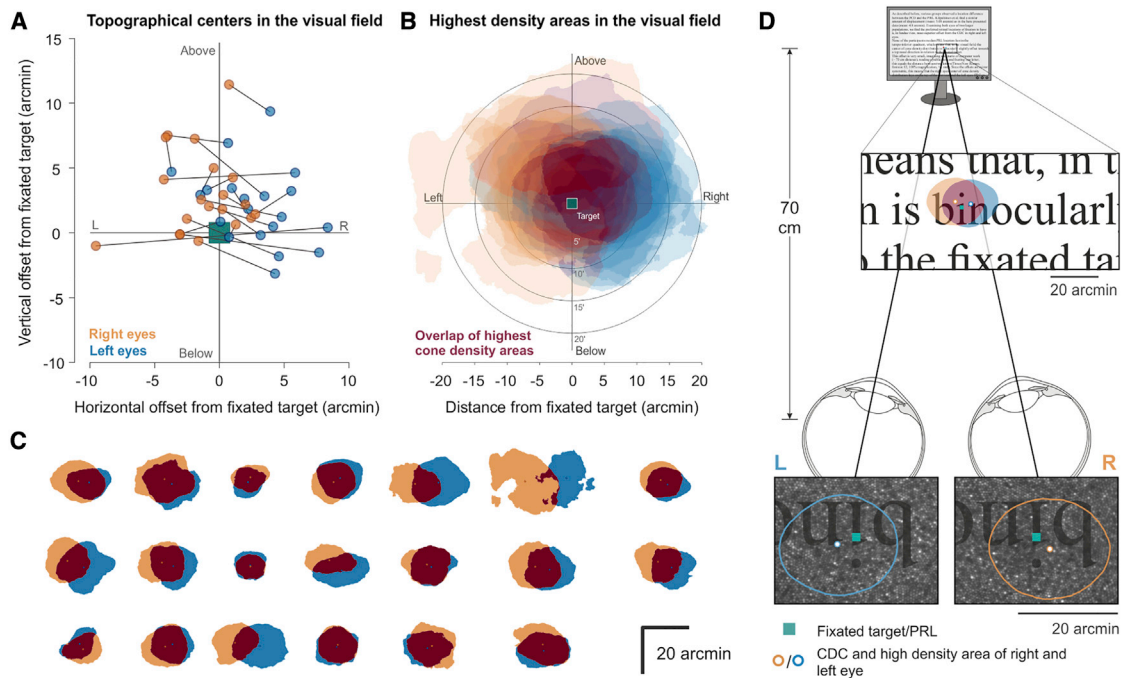


Figure 4. Projection of cone topography into the binocular visual field

(A) CDC of both eyes (right, orange; left, blue) plotted with their PRL as common center in the visual field. Lines connect fellow eyes. (B) Similar as in (A), including retinal areas encompassing the highest 20% cone densities (within the central 50 arcmin of the fovea). Overlap is shown in dark red. (C) Projections of high-density cone areas of all participants. (D) The average displacement between fellow eyes, in a static reading situation, roughly equals the distance between two letters at reading distance (~1 mm). Orientation of cone mosaics is as seen from behind the observer.

● **METHOD DETAILS**

- Adaptive optics retinal imaging
- Image processing and cone density analysis
- Determination of the preferred retinal location of fixation (PRL)

● **QUANTIFICATION AND STATISTICAL ANALYSIS**

SUPPLEMENTAL INFORMATION

Supplemental information can be found online at <https://doi.org/10.1016/j.cub.2021.07.005>.

ACKNOWLEDGMENTS

We thank Austin Roorda and the members of his lab for kindly providing image and PRL data for re-analysis. We are grateful for insightful comments by the reviewers of an earlier version of this manuscript. This work was supported by the Carl Zeiss Foundation (HC-AOSLO) and the Emmy Noether Program of the German Research Foundation (DFG) (Ha 5323/5-1).

AUTHOR CONTRIBUTIONS

J.L.R. and W.M.H. conceived the research idea. J.L.R., N.D., and W.M.H. developed the data analysis pipeline. J.L.R. performed the data analysis and convolutional neural network training. J.L.R. and W.M.H. wrote the manuscript. All authors discussed the results and edited the manuscript.

DECLARATION OF INTERESTS

The authors declare no competing interests.

Received: April 1, 2021
Revised: May 28, 2021
Accepted: July 2, 2021
Published: August 2, 2021

REFERENCES

1. Cava, J.A., Allphin, M.T., Mastey, R.R., Gaffney, M., Linderman, R.E., Cooper, R.F., and Carroll, J. (2020). Assessing interocular symmetry of the foveal cone mosaic. *Invest. Ophthalmol. Vis. Sci.* 61, 23.
2. Wang, Y., Bensaid, N., Tiruveedhula, P., Ma, J., Ravikumar, S., and Roorda, A. (2019). Human foveal cone photoreceptor topography and its dependence on eye length. *eLife* 8, e47148.
3. Curcio, C.A., Sloan, K.R., Kalina, R.E., and Hendrickson, A.E. (1990). Human photoreceptor topography. *J. Comp. Neurol.* 292, 497–523.
4. Zhang, C., Kim, Y.J., Silverstein, A.R., Hoshino, A., Reh, T.A., Dacey, D.M., and Wong, R.O. (2020). Circuit reorganization shapes the developing human foveal midget connectome toward single-cone resolution. *Neuron* 108, 905–918.e3.
5. Bryman, G.S., Liu, A., and Do, M.T.H. (2020). Optimized signal flow through photoreceptors supports the high-acuity vision of primates. *Neuron* 108, 335–348.e7.
6. Poletti, M., Listorti, C., and Rucci, M. (2013). Microscopic eye movements compensate for nonhomogeneous vision within the fovea. *Curr. Biol.* 23, 1691–1695.
7. Poletti, M., Rucci, M., and Carrasco, M. (2017). Selective attention within the foveola. *Nat. Neurosci.* 20, 1413–1417.
8. Ko, H.K., Poletti, M., and Rucci, M. (2010). Microsaccades precisely relocate gaze in a high visual acuity task. *Nat. Neurosci.* 13, 1549–1553.

9. Putnam, N.M., Hofer, H.J., Doble, N., Chen, L., Carroll, J., and Williams, D.R. (2005). The locus of fixation and the foveal cone mosaic. *J. Vis.* **5**, 632–639.
10. Wilk, M.A., Dubis, A.M., Cooper, R.F., Summerfelt, P., Dubra, A., and Carroll, J. (2017). Assessing the spatial relationship between fixation and foveal specializations. *Vision Res.* **132**, 53–61.
11. Harmening, W.M., Tuten, W.S., Roorda, A., and Sincich, L.C. (2014). Mapping the perceptual grain of the human retina. *J. Neurosci.* **34**, 5667–5677.
12. Rossi, E.A., and Roorda, A. (2010). The relationship between visual resolution and cone spacing in the human fovea. *Nat. Neurosci.* **13**, 156–157.
13. Sincich, L.C., Zhang, Y., Tiruveedhula, P., Horton, J.C., and Roorda, A. (2009). Resolving single cone inputs to visual receptive fields. *Nat. Neurosci.* **12**, 967–969.
14. Sprague, W.W., Cooper, E.A., Tošić, I., and Banks, M.S. (2015). Stereopsis is adaptive for the natural environment. *Sci. Adv.* **1**, e1400254.
15. Gibaldi, A., and Banks, M.S. (2019). Binocular eye movements are adapted to the natural environment. *J. Neurosci.* **39**, 2877–2888.
16. Li, K.Y., Tiruveedhula, P., and Roorda, A. (2010). Intersubject variability of foveal cone photoreceptor density in relation to eye length. *Invest. Ophthalmol. Vis. Sci.* **51**, 6858–6867.
17. Zhang, T., Godara, P., Blanco, E.R., Griffin, R.L., Wang, X., Curcio, C.A., and Zhang, Y. (2015). Variability in human cone topography assessed by adaptive optics scanning laser ophthalmoscopy. *Am. J. Ophthalmol.* **160**, 290–300.e1.
18. Cooper, R.F., Wilk, M.A., Tarima, S., and Carroll, J. (2016). Evaluating descriptive metrics of the human cone mosaic. *Invest. Ophthalmol. Vis. Sci.* **57**, 2992–3001.
19. Wells-Gray, E.M., Choi, S.S., Bries, A., and Doble, N. (2016). Variation in rod and cone density from the fovea to the mid-periphery in healthy human retinas using adaptive optics scanning laser ophthalmoscopy. *Eye (Lond.)* **30**, 1135–1143.
20. Packer, O., Hendrickson, A.E., and Curcio, C.A. (1989). Photoreceptor topography of the retina in the adult pigtail macaque (*Macaca nemestrina*). *J. Comp. Neurol.* **288**, 165–183.
21. Wikler, K.C., Williams, R.W., and Rakic, P. (1990). Photoreceptor mosaic: number and distribution of rods and cones in the rhesus monkey retina. *J. Comp. Neurol.* **297**, 499–508.
22. Park, S.P., Chung, J.K., Greenstein, V., Tsang, S.H., and Chang, S. (2013). A study of factors affecting the human cone photoreceptor density measured by adaptive optics scanning laser ophthalmoscope. *Exp. Eye Res.* **108**, 1–9.
23. Mirhajianmoghadam, H., Jnawali, A., Musial, G., Queener, H.M., Patel, N.B., Ostrin, L.A., and Porter, J. (2020). In vivo assessment of foveal geometry and cone photoreceptor density and spacing in children. *Sci. Rep.* **10**, 8942.
24. Yuodelis, C., and Hendrickson, A. (1986). A qualitative and quantitative analysis of the human fovea during development. *Vision Res.* **26**, 847–855.
25. Lai, Y.H., Wang, H.Z., and Hsu, H.T. (2011). Development of visual acuity in preschool children as measured with Landolt C and Tumbling E charts. *J. AAPOS* **15**, 251–255.
26. Lu, R., Aguilera, N., Liu, T., Liu, J., Giannini, J.P., Li, J., Bower, A.J., Dubra, A., and Tam, J. (2021). *In-vivo* sub-diffraction adaptive optics imaging of photoreceptors in the human eye with annular pupil illumination and sub-Airy detection. *Optica* **8**, 333–343.
27. Castejón-Mochón, J.F., López-Gil, N., Benito, A., and Artal, P. (2002). Ocular wave-front aberration statistics in a normal young population. *Vision Res.* **42**, 1611–1617.
28. Lombardo, M., Lombardo, G., Schiano Lomoriello, D., Ducoli, P., Stirpe, M., and Serrao, S. (2013). Interocular symmetry of parafoveal photoreceptor cone density distribution. *Retina* **33**, 1640–1649.
29. Reiniger, J.L., Domdei, N., Linden, M., Holz, F.G., and Harmening, W.M. (2019). Relationship between the foveal photoreceptor mosaic and adaptive optics corrected visual acuity. *Invest. Ophthalmol. Vis. Sci.* **60**, 1777.
30. Reiniger, J.L., Lobecke, A.C., Sabesan, R., Bach, M., Verbakel, F., de Brabander, J., Holz, F.G., Berendschot, T.T.J.M., and Harmening, W.M. (2019). Habitual higher order aberrations affect Landolt but not Vernier acuity. *J. Vis.* **19**, 11.
31. Polyak, S., and Willmer, E.N. (1949). Retinal structure and colour vision. *Doc. Ophthalmol.* **3**, 24–56.
32. Kilpeläinen, M., Putnam, N.M., Ratnam, K., and Roorda, A. (2020). The anatomical, functional and perceived location of the fovea in the human visual system. *Curr. Biol.* Published online October 9, 2020. <https://doi.org/10.2139/ssrn.3699785>.
33. Domdei, N., Reiniger, J.L., Holz, F.G., and Harmening, W.M. (2021). The relationship between visual sensitivity and eccentricity, cone density and outer segment length in the human foveola. *Invest. Ophthalmol. Vis. Sci.* **62**, 31.
34. Krauskopf, J., Cornsweet, T.N., and Riggs, L.A. (1960). Analysis of eye movements during monocular and binocular fixation. *J. Opt. Soc. Am.* **50**, 572–578.
35. González, E.G., Wong, A.M.F., Niechwiej-Szwedo, E., Tarita-Nistor, L., and Steinbach, M.J. (2012). Eye position stability in amblyopia and in normal binocular vision. *Invest. Ophthalmol. Vis. Sci.* **53**, 5386–5394.
36. Zhu, X., He, W., Du, Y., Zhang, K., and Lu, Y. (2019). Interocular symmetry of fixation, optic disc, and corneal astigmatism in bilateral high myopia: the Shanghai high myopia study. *Transl. Vis. Sci. Technol.* **8**, 22.
37. Hillis, J.M., and Banks, M.S. (2001). Are corresponding points fixed? *Vision Res.* **41**, 2457–2473.
38. Home, R. (1978). Binocular summation: a study of contrast sensitivity, visual acuity and recognition. *Vision Res.* **18**, 579–585.
39. Gibaldi, A., Labhishetty, V., Thibos, L.N., and Banks, M.S. (2021). The blur horopter: retinal conjugate surface in binocular viewing. *J. Vis.* **21**, 8.
40. Rucci, M., Iovin, R., Poletti, M., and Santini, F. (2007). Miniature eye movements enhance fine spatial detail. *Nature* **447**, 851–854.
41. Ratnam, K., Domdei, N., Harmening, W.M., and Roorda, A. (2017). Benefits of retinal image motion at the limits of spatial vision. *J. Vis.* **17**, 30.
42. Rucci, M., Ahissar, E., and Burr, D. (2018). Temporal coding of visual space. *Trends Cogn. Sci.* **22**, 883–895.
43. Stanford, L.R. (1987). Conduction velocity variations minimize conduction time differences among retinal ganglion cell axons. *Science* **238**, 358–360.
44. Dacey, D.M. (1993). The mosaic of midget ganglion cells in the human retina. *J. Neurosci.* **13**, 5334–5355.
45. Tan, G., Lee, Y.-H., Zhan, T., Yang, J., Liu, S., Zhao, D., and Wu, S.-T. (2018). Foveated imaging for near-eye displays. *Opt. Express* **26**, 25076–25085.
46. Song, H., Rossi, E.A., and Williams, D.R. (2021). Reduced foveal cone density in early idiopathic macular telangiectasia. *BMJ Open Ophthalmol.* **6**, e000603.
47. Cunefare, D., Fang, L., Cooper, R.F., Dubra, A., Carroll, J., and Farsiu, S. (2017). Open source software for automatic detection of cone photoreceptors in adaptive optics ophthalmoscopy using convolutional neural networks. *Sci. Rep.* **7**, 6620.
48. Roorda, A., Romero-Borja, F., Donnelly III, W., Queener, H., Hebert, T., and Campbell, M. (2002). Adaptive optics scanning laser ophthalmoscopy. *Opt. Express* **10**, 405–412.
49. Domdei, N., Domdei, L., Reiniger, J.L., Linden, M., Holz, F.G., Roorda, A., and Harmening, W.M. (2017). Ultra-high contrast retinal display system for single photoreceptor psychophysics. *Biomed. Opt. Express* **9**, 157–172.
50. Poonja, S., Patel, S., Henry, L., and Roorda, A. (2005). Dynamic visual stimulus presentation in an adaptive optics scanning laser ophthalmoscope. *J. Refract. Surg.* **21**, S575–S580.
51. Arathorn, D.W., Yang, Q., Vogel, C.R., Zhang, Y., Tiruveedhula, P., and Roorda, A. (2007). Retinally stabilized cone-targeted stimulus delivery. *Opt. Express* **15**, 13731–13744.
52. Bruce, K.S., Harmening, W.M., Langston, B.R., Tuten, W.S., Roorda, A., and Sincich, L.C. (2015). Normal perceptual sensitivity arising from weakly reflective cone photoreceptors. *Invest. Ophthalmol. Vis. Sci.* **56**, 4431–4438.

STAR★METHODS

KEY RESOURCES TABLE

REAGENT or RESOURCE	SOURCE	IDENTIFIER
Deposited data		
Raw and analyzed data	This paper	https://doi.org/10.17632/9gkpxsmz23.1
Software and algorithms		
MATLAB R2016a (Data analysis)	MathWorks	https://www.mathworks.com
CNN-Cone-Detection	Cunefare et al. ⁴⁷	https://github.com/DavidCunefare/CNN-Cone-Detection
Other		
Re-analyzed data	Wang et al. ²	https://doi.org/10.5061/dryad.nh0fp1b

RESOURCE AVAILABILITY

Lead contact

Further information and requests for resources should be directed to and will be fulfilled by the Lead Contact, Wolf M. Harmening (wolf.harmening@ukbonn.de).

Materials availability

This study did not generate new unique reagents.

Data and code availability

Cone mosaic images, cone coordinates and retinal locations (PCD, CDC and PRL) have been deposited at Mendeley Data and are publicly available as of the date of publication. A MATLAB code that can be used for plotting the data on the original image is provided. This paper analyzes existing, publicly available data. The access links and DOIs for the datasets and code are listed in the [Key resources table](#).

EXPERIMENTAL MODEL AND SUBJECT DETAILS

Human participants

Forty-one eyes of twenty-one participants (7 male, 14 female, 18 adults [age: 18 – 42], 3 children [age: 10, 12 and 14]) with no known ocular conditions and only mild refractive errors (SE: \pm 2.5 diopters) were studied. Participants are referred to throughout the manuscript with a singular ID, selected based on a descending order of peak cone densities for the left eye. For one of the participants (P21), data from the right eye were included as the only monocular dataset in the study, because the left eye's cone mosaic could not be resolved completely. Therefore, this eye's data were only used for PRL reproducibility analysis, as image and functional data were collected over multiple years. Most of the participants were examined on multiple days (compare [Table S1](#)). Participants P4, P13 and P21 were trained AOSLO observers and members of the lab. Mydriasis was established by two drops of 1% Tropicamide, instilled into the eyelid about 15 and 10 minutes prior to the imaging session. A third drop was administered in case imaging and experimentation continued for more than 30 minutes. A customized dental impression mold (bite bar) was used to immobilize and adjust the head position and thus to align the participants eye in front of the imaging system. Written informed consent was obtained from each participant and all experimental procedures adhered to the tenets of the Declaration of Helsinki, in accordance with the guidelines of the independent ethics committee of the medical faculty at the Rheinische Friedrich-Wilhelms-Universität of Bonn.

METHOD DETAILS

Adaptive optics retinal imaging

In vivo images of the complete foveolar cone mosaic were recorded using a custom-built adaptive optics scanning laser ophthalmoscope (AOSLO). The general setup of the AOSLO has been described previously,^{48,49} pertinent differences are described here. Briefly, the AOSLO front-end featured three $f = 500$ mm afocal telescopes, designed to point-scan an adaptive optics corrected focal spot of light across the retina to achieve diffraction limited resolution performance in both the incident and reflected beams. A magnetic actuator-driven deformable mirror with continuous membrane surface (DM97-07, 7.2 mm pupil diameter, ALPAO, Montbonnot-Saint-Martin, France) was placed in a retinal conjugate plane and driven by the error signals of a 25x25 lenslet Shack Hartmann

sensor (SHSCam AR-S-150-GE, Optocraft GmbH, Erlangen, Germany). Imaging and wavefront correction wavelength was either 840 nm (± 12 nm) or 788 nm (± 12 nm) light, obtained by serial dichroic and bandpass filtering of a supercontinuum source (SuperK Extreme EXR-15, NKT Photonics, Birkerød, Denmark). The imaging field of view was 0.85×0.85 degree of visual angle. The light reflected from the retina was captured in a photomultiplier tube (PMT, H7422-50, Hamamatsu Photonics, Hamamatsu, Japan), placed behind a confocal pinhole (Pinhole diameter = 20 μm , equaling 0.47 (840nm) and 0.5 (788nm) Airy disk diameters). The PMT signal was sampled continuously in a field programmable gate array (FPGA), rendering a 512×512 pixel video at 30 Hz (600 pixel per degree of visual angle). With fast acousto-optic modulation of the imaging wavelengths, the square imaging field becomes a retinal display in which psychophysical visual stimulation was possible.^{11,50} The best images during PRL recordings (see below) were used to create spatially registered, high signal to noise ratio images of the foveal center in which all cones could be resolved.

Image processing and cone density analysis

Acquired AOSLO video frames were spatially stabilized by real-time, strip-wise image registration in custom written software.⁵¹ These online-stabilized videos contained frames displaying incomplete stabilization that could be due to poor image quality, eye blinks, drying tear film, etc. Such frames were identified and deleted manually. The remaining frames were averaged to obtain a single high-quality image of each retina per video. The single best of at least five such images was selected to be used for further analysis and serve as high signal-to-noise anchor image for spatial alignment with functional data recordings. All cone center locations were labeled in a semi-manual process by a single trained image grader: first, a convolutional neural network,⁴⁷ CNN, was trained to locate cone center locations with a smaller subset of only manually graded images in our pilot study. Then, all retinal images were annotated by the newly trained CNN, and manually corrected using custom software. Such corrections were especially necessary in the foveal center, and wherever cones appeared completely dark.⁵² The manual correction prioritized mosaic regularity in cases of ambiguity.³ Based on the labeled cone center locations, a Voronoi tessellation was computed (MATLAB functions: *delatunayTriangulation*, *voronoiDiagram* and *voronoin*). Each cone was regarded as occupying the space of each corresponding Voronoi cell. Angular cone density (cones/deg²) was computed at each image pixel by averaging the Voronoi area of the nearest 150 encircled cones around that pixel (Figure 1D). This method ensured smooth cone density maps and prevented sampling artifacts as they often occur using defined shapes of masks (e.g., circular or square masks) for selection of cones in a particular area (Figure 1E). Linear cone densities were computed with respect to the individual retinal magnification factors of each eye, considering axial length, anterior chamber depth and corneal curvature,¹⁶ based on swept source biometry (IOLMaster 700, Carl Zeiss Meditech, Jena, Germany). Finally, the cone density centroid (CDC) was determined as the weighted centroid (MATLAB function: *regionprops(region_logical, image, "WeightedCentroid")*) of the highest 20% of cone density values. The CDC is indicated by circular marker throughout the manuscript. The 20th percentile was chosen arbitrarily because the entire contour was evaluable in all eyes. CDC locations did only marginally change at other contours. At the 20% contour, cone densities equaled the highest $\sim 13\%$ of densities across the entire retina, considering previously reported cone densities at larger retinal eccentricities.^{3,19} Therefore, the theoretical limit of cone sampling within those areas was < 35 arcsec (range: 9600 to 14900 cones/deg²), equaling 20/13 vision or better under correction of ocular aberrations. Under natural viewing conditions, expected performance would be slightly less due to higher order aberrations and crucially depends on post-receptor circuitry, midgen bipolar and ganglion cells (see Discussion).

To quantify overall symmetry between density maps, three different analyses were performed:

- (1) Spatial two-dimensional differences (or reproducibility) of cone density maps of the same eye were recorded and analyzed independently on different days (columns in Figures S2A and S2B), based on a careful alignment of the cone mosaic images.
- (2) The differences between density maps of fellow eyes which were recorded on the same day (rows in Figures S2A and S2B) were obtained by comparing flipping the left eyes map along the vertical axis and aligning it with the CDC of the right eyes map.
- (3) The difference between individual density maps of all right eyes and a randomly selected left eye, which was flipped and aligned with the CDC of the right eye as described in analysis (2).

To quantify the two-dimensional differences, the root-mean-square (RMS) of the point-by-point difference maps was used for the comparison between absolute and normalized density maps (Figure S2C, respectively, compare with Figure 1G and 1H).

Determination of the preferred retinal location of fixation (PRL)

Using the AOSLO as stimulation platform, a small (nominal 1.6 arcmin), flashing (3 Hz) square with negative contrast polarity (light turned off) was presented as visual target at the center of the AOSLO imaging raster during image acquisition, and participants were asked to fixate the target as accurately and relaxed as possible. At least five 10 s AOSLO videos were recorded in each eye during such fixation epochs. In AOSLO videos, the visual stimulus was directly visible with respect to the retina (Figures 2A and 3B). Thus, fixation behavior can be directly and unambiguously observed in such videos. The PRL was calculated as the median fixation target location across all videos. To bring fixation behavior into spatial correspondence with the topographical analysis, averaged retinal images derived from both analyses independently were carefully aligned with each other. In 33 of the 41 eyes, PRL measurements were conducted multiple times (e.g., if participants also took part in other experiments). In three eyes (P13, P4 and P21), data were obtained in 8, 12 and 17 measurement sessions, respectively, over a period of 3.5 years. For eight participants (16 eyes)

sessions were repeated after 1 year. For quantification of fixation stability, the isoline area (ISOA) which contains one standard deviation (STD) of the data was fitted to the scatterplot of all stimulus positions (Figure 2B).

QUANTIFICATION AND STATISTICAL ANALYSIS

All statistical analyses were performed using MATLAB v2016.